ACS APPLIED MATERIALS & INTERFACES
Research Article
www.acsami.org

In Situ Self-Sacrificed Template Synthesis of Fe-N/G Catalysts for Enhanced Oxygen Reduction

Qingxue Lai,[†] Qi Su,[†] Qingwen Gao,[†] Yanyu Liang,*[,†] Yuxi Wang,[‡] Zhi Yang,*[,‡] Xiaogang Zhang,[†] Jianping He,[†] and Hao Tong[†]

[†]College of Materials Science and Technology, Nanjing University of Aeronautics and Astronautics, Nanjing, 210016, P. R. China
[‡]Key Laboratory for Thin Film and Microfabrication of Ministry of Education, Department of Micro/Nano Electronics, School of Electronic Information and Electrical Engineering, Shanghai Jiao Tong University, Shanghai 200240, P. R. China

Supporting Information

ABSTRACT: To facilely prepare high-performance Fe-N/G oxygen reduction catalysts via a simple and controllable route from available and low-cost materials is still a challenge. Herein, we develop an *in situ* self-sacrificed template strategy to synthesize Fe-N/G catalysts from melamine, glucose, and $FeSO_4 \cdot 7H_2O$. Fe/Fe_3C@graphitic carbon nanocapsules are uniformly formed on the NG surface to create a highly opened and stable mesoporous framework structure. Furthermore, effectively doped N sites and high active Fe-N_x sites are synchronously constructed on such structures, leading to an enhanced synergistic effect for ORR and promising the Fe-N/G catalyst a similar catalytic activity and four-electron selectivity, but superior stability to commercial 30 wt % Pt/C catalysts in 0.1 M KOH solution under the same loading.

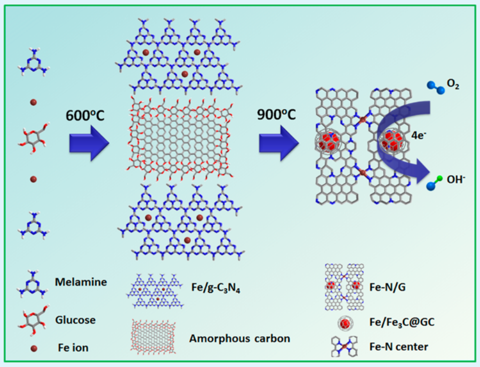

KEYWORDS: *in situ self-sacrificed template, Fe-N/G catalyst, synergistic effect, oxygen reduction reaction, fuel cell*

1. INTRODUCTION

The commercial applications of fuel cell technologies are still mostly limited by high cost due to their exclusive use of expensive platinum group metal (PGM)-based catalysts, especially for the cathodic oxygen reduction reaction (ORR) with slow kinetics.[1−3] Searching cheap and efficient non-PGM catalysts for ORR has been considered as an effective method to eliminate this predicament.[4,5] However, progress toward developing non-PGM catalysts was slow since transition metal phthalocyanines were used as the first non-PGM ORR catalysts.[6] In recent years, increasing efforts have been devoted to this research subject and many kinds of novel non-PGM catalysts are achieved, including transition metal oxides,[7,8] doped nanocarbon,[9,10] and their hybrids.[11,12] Especially for nanocarbon-based catalysts, it has been revealed that heteroatoms (e.g., nitrogen, boron, sulfur, and phosphorus) in nanocarbon frameworks can effectively activate π electrons of sp^2-hybridized carbon to create novel metal-free ORR active sites.[13,14] This remarkable discovery opens a new chapter in the development of non-PGM catalysts. Further research demonstrates that introducing a transition metal (TM), especially Fe, into the nitrogen-doped nanocarbon framework to form Fe-N/C catalysts can generate strong synergistic catalysis for ORR, which results into a novel non-PGM catalyst system with improved electrocatalytic performance.[15−17] As a result, these low-cost and efficient catalyst systems have been considered as one of the most promising PGM substitutes and provide an increasing possibility for the large-scale commercialization of next-generation fuel cells.

Even though the ORR catalytic mechanism on Fe-N/C has not been completely uncovered, a consensus has been reached that an iron center coordinated with nitrogen atoms (Fe-N_x) is more responsible for the excellent catalytic performance.[18,19] Current research is focusing on the high efficient doping of Fe and N on highly opened and stable carbon supports, especially a graphene framework (formed Fe-N/G) due to its prominent advantages from the special two-dimensional structure.[20] One efficient strategy to synthesize high-performance Fe-N/G ORR catalyst is postfunctionalization of graphene oxide (GO) with metal and nitrogen precursors, followed by pyrolysis treatment. For example, Parvez et al. reported NG/Fe_x catalysts prepared through thermolysis of GO, $FeCl_3$, and cyanamide at high temperature, which have outperformed Pt/C toward ORR in both acidic and alkaline media.[21] Although the synthesis process is convenient, the powerful dependency on GO makes it difficult and time-consuming to synthesize currently. To avoid the dependency on GO, a bottom-up synthesis strategy is much desired, which could achieve the synchronous construction of the graphene framework as well as the active Fe-N_x sites. For example, Peng et al. reported a Fe- and N- doped carbon catalyst Fe-PANI/C-Mela with a graphene structure via

Received: June 30, 2015
Accepted: July 29, 2015
Published: July 29, 2015

DOI: 10.1021/acsami.5b05834

Scheme 1. *In Situ* Self-Sacrificed Template Synthesis Strategy for Fe-N/G Catalysts

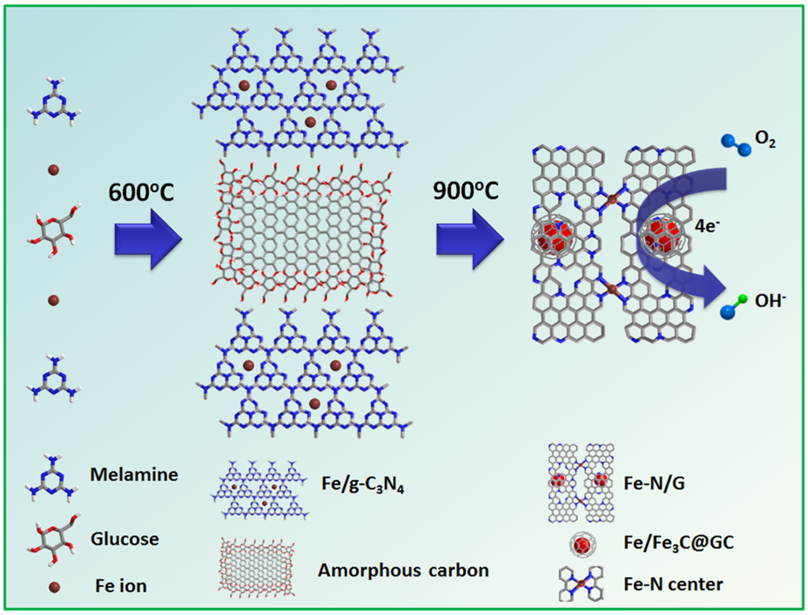

pyrolysis of polyaniline (PANI) with melamine and an iron precursor.[22] Even though the formation mechanism is not further revealed, such a bottom-up strategy is more effective for the synthesis of catalysts and more conducive to large-scale production when compared with the conventional route via postfunctionalization of graphene oxide. However, the obtained catalysts showed excitingly high ORR activity but low stability in a H_2-air single fuel cell test. The obvious decay of the activity is probably attributed to the serious restacking of the graphene structure, which is an inevitable problem during the usage of graphene-based nanomaterials.[23] Therefore, performing a simple and efficient bottom-up synthetic route to synthesize high-performance Fe-N/G catalysts with a highly opened and stable structure from available materials is strongly desired but remains greatly challenging.

Thanks to the fast development of the bottom-up synthesis of graphene,[24,25] it makes it more possible to achieve high-performance Fe-N/G catalysts via this method. Herein, we employ an *in situ* self-sacrificed template strategy to bottom-up fabricate Fe-N/G catalysts from available and low-cost materials. Evenly distributed Fe/Fe_3C@graphitic carbon nanocapsules are uniformly formed on the surface of graphene, which can effectively prevent the graphene structure from stacking and keep the catalytic activity stable. Furthermore, efficient doping of nitrogen with pyridinic and graphitic types as well as formation of abundant Fe(II)-N_4/CFe(II)-N_2 active sites promises the prepared Fe-N/G catalysts with comparable catalytic activity, four-electron selectivity, but super stability in 0.1 M KOH solution under the same loading. Such an *in situ* 2D self-sacrificed template strategy can effectively avoid the complex synthesis processes of the conventional template method and will hold great potential for the industrial manufacture of microstructure-controllable Fe-N/C catalysts for ORR.

2. EXPERIMENTAL SECTION

2.1. Preparation of NG, Fe-N/G, and Fe-NG Catalysts. In a typical procedure, 4.000 g of melamine, 100 mg of glucose, and 20 mg of $FeSO_4 \cdot 7H_2O$ were mixed together by grinding to form a uniform white mixture. For heat treatment of the mixture, it was placed in a crucible with a lid and treated in a tubular furnace under a N_2 atmosphere at 600 °C for 3 h, followed by annealing at 900 °C for 1 h. Subsequently, the furnace was cooled to room temperature slowly and Fe-N/G catalysts with N- and Fe-N_x-doped sites were obtained without other post-treatment. NG was prepared using the similar route without adding an iron source. A Fe-NG catalyst without Fe-N_x-doped sites was also prepared via heat treat of NG (obtained from pyrolysis of 4.000 g of melamine and 0.100 g of glucose at 900 °C) with 20 mg of $FeSO_4 \cdot 7H_2O$ under the same conditions. Fe-N/G with other Fe loadings are facilely synthesized by adjusting the addition of Fe precursor with a fixed amount of glucose (100 mg) (10, 20, and 40 mg with a weight ratio of Fe precursor/glucose at 10, 20, and 40%, respectively). The Fe-N/G (or Fe-NG) in this paper without other instructions is referred to as the Fe-N/G (or Fe-NG) with a weight ratio of Fe precursor/glucose at 20%.

2.2. Structural Characterizations. The composition was examined by an XRD instrument (Rigaku Corporation D/max-2200/PC). The Raman spectra were recorded on a Bruker Optics, Senterra R200-L spectrometer (Germany) with excitation by an argon ion laser (532 nm). The morphology and microstructure were investigated by TEM (Philips Tecnai 12), HRTEM (Philips Tecnai G2), and STEM (FEI Tecnai G2 F30 S-TWIN) transmission electron microscopes. The surface elemental composition was determined by XPS (Kratos AXIS Ultra) measurements. The porous structures were conducted with a Micrometrics ASAP2020 analyzer (USA) at 77 K. TG was tested on a NETZSCH STA 409TG thermobalance (Germany) with a heat rate of 10 °C/min under air. Mössbauer spectra were recorded at room temperature in the transmission mode using an MS 500 (Oxford Instruments, U.K.) with a 57Co/Pd-source, and the calibration is made with respect to α-Fe.

2.3. Electrochemical Measurements. A 1.0 mg portion of the prepared catalyst (NG, Fe-N/G, Fe-NG) or commercial 30 wt % Pt/C catalyst was dispersed in 1.00 mL of 0.05 wt % Nafion ethanol solution and sonicated for about 45 min to form a homogeneous ink solution. The electrode was prepared by dropping 10.0 μL of ink solution of the prepared catalysts or commercial 30 wt % Pt/C on a RDE glass carbon electrode with a diameter of 5.00 mm (12.6 μL for RRDE glass carbon electrode with a diameter of 5.61 mm) and dried under room temperature. Electrochemical measurements were conducted using a three-electrode cell with a saturated calomel electrode (SCE), and a platinum sheet was used as the reference and counter electrodes, respectively. ORR tests were carried out in O_2- or N_2-saturated 0.1 M KOH electrolyte at room temperature on a CHI760D electrochemical workstation assembled with an MSR Electrode Rotator (Pine Research

Instrumentation). The electrode potential is calibrated based on the equation: E (RHE) = E (SCE) + 0.99 V. The electrochemical active surface area (EASA) for NG, Fe-N/G, and Fe-NG is calculated by integrating the CV curve recorded in N_2-saturated 0.1 M KOH electrolyte. Considering that the absorption/desorption of hydrogen occurs for commercial 30 wt % Pt/C, the integration integral is chosen from 0.35 to 0.50 V vs RHE. The four-electron selectivity of catalysts was evaluated based on the HO_2^- yield and electron transfer number (n), calculated from the following equations:

$$HO_2^-(\%) = 200 \times \frac{I_R/N}{I_R/N + I_D} \quad (1)$$

$$n = 4 \times \frac{I_D}{I_R/N + I_D} \quad (2)$$

Here, I_D and I_R are the disk and ring currents, respectively, and N is the ring collection efficiency (0.37).

3. RESULTS AND DISCUSSION

3.1. Physical Characterization of the Prepared NG, Fe-N/G, and Fe-NG Catalysts. The *in situ* self-sacrificed template synthesis strategy for Fe-N/G catalysts is illustrated in Scheme 1. Melamine-derived graphitic carbon nitride (g-C_3N_4) was formed at 600 °C under a nitrogen atmosphere to serve as the *in situ* two-dimensional (2D) self-sacrificed template. When glucose and ferrous sulfate ($FeSO_4{\cdot}7H_2O$) were incorporated as the precursors of carbon and iron, respectively, the highly opened and stable Fe-N/G catalyst was obtained after the complete decomposition of g-C_3N_4 at 900 °C, without any post-treatment.

The intermediate product from pyrolysis of melamine, glucose, and $FeSO_4{\cdot}7H_2O$ at 600 °C is characterized by the X-ray diffraction (XRD) pattern, transmission electron microscopy (TEM), and X-ray photoelectron spectroscopy (XPS). The XRD pattern in Figure 1a shows a typical g-C_3N_4 phase without any impurity peak,[26] suggesting that melamine is polymerized to g-C_3N_4 at this temperature and the amorphous carbon as well as iron-contained phases is too little to be detected by XRD analysis. The TEM image in Figure 1b presents a 2D layer morphology with abundant wrinkles, and no metal particles are observed on it. XPS analysis in Figure 1c−f demonstrates that, except for the C═C (284.55 eV), C−C/O (285.35 eV), and C═O (286.61 eV) bonds usually observed in amorphous carbon, there are still abundant C−N (288.25 eV) and C═N (288.77 eV) bonds in the intermediate product; meanwhile, only pyridinic (400.26 eV) and graphitic (402.08 eV) type N atoms are observed, which is in well accordance with the structure of g-C_3N_4.[27] Therefore, it can be considered that the glucose-derived amorphous carbon coexists with g-C_3N_4 in the intermediate product. Because of the extreme excess of 2D g-C_3N_4 structures, the amorphous carbon must be confined in the layer space of g-C_3N_4. Furthermore, Fe^{2+} and Fe^{3+} are detected by XPS, but there is no corresponding O−Fe bond (529.5 eV) in the O 1s spectrum,[28] suggesting that the metal ions are probably strongly complexed with g-C_3N_4 to form Fe−N bonds.[29] However, no obvious Fe−N signals are observed in the high-resolution N 1s XPS spectrum. Because of the very low molar ratio of $FeSO_4{\cdot}7H_2O$/melamine (1:446.7), it can be supposed that the weak Fe−N signals are mostly covered by strong signals from abundant pyridinic- and graphitic-type N bonds of g-C_3N_4, making it hard to distinguish the former from the latter by XPS analysis.

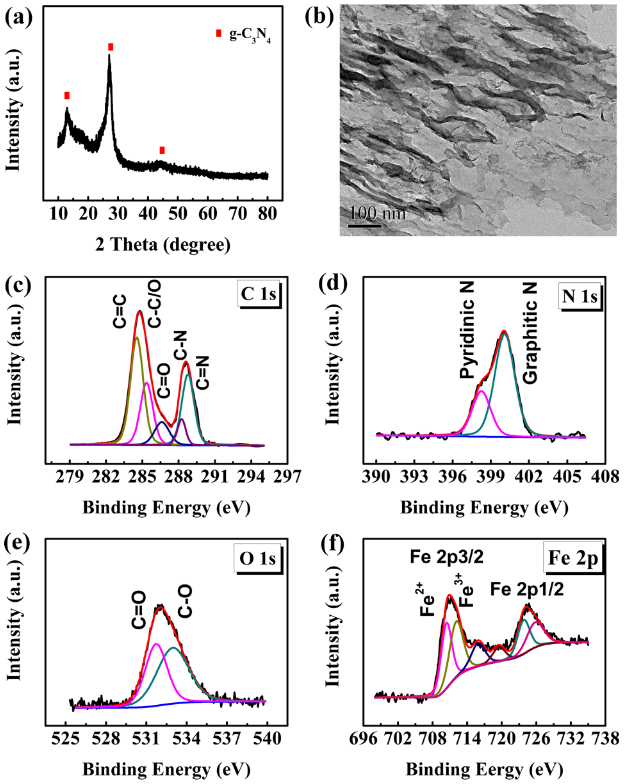

Figure 1. Physical characterization of the intermediate product from pyrolysis of melamine, glucose, and $FeSO_4{\cdot}7H_2O$ at 600 °C. (a) XRD pattern; (b) TEM image; and high-resolution XPS spectra of (c) C 1s, (d) N 1s, (e) O 1s, and (f) Fe 2p.

The Fe-N/G catalyst is achieved after pyrolysis at 900 °C under a nitrogen atmosphere. The yield is about 20−40% (calculated based on added carbon from glucose) with increasing the weight ratio of $FeSO_4{\cdot}7H_2O$/glucose from 10% to 40%. As shown in Figure 2a, the Fe-N/G catalyst has evident diffraction peaks of the graphitic carbon (002) plane at 26.2° and α-Fe (JCPDS, No. 87-0722) at 44.8° and 65.1°. The rest of the diffraction peaks are corresponding to the Fe_3C phase (JCPDS, No. 89-2867).[30] In addition, the C (002) diffraction peak of Fe-N/G becomes more sharp than that of NG and Fe-NG. These results suggest an enhanced crystallinity degree of the carbon phase from the *in situ* catalytic graphitization effect of Fe/Fe_3C.[31]

The low-resolution bright-field and dark-field TEM images of Fe-N/G in Figure 2b,c clearly indicate that the high-contrast Fe/Fe_3C nanoparticles (NPs) with smooth edges and an average diameter of 19.3 nm are homogeneously distributed on the surface of NG, which has abundant folded structures. On the contrary, no metallic nanoparticles are observed on the surface of pure NG, as shown in Figure 2g and Figure S1. The high-resolution TEM images in Figure 2d−f further demonstrate that the NG support has many exposed nanoedges, which can provide highly positive spin and/or charge densities to facilitate oxygen adsorption.[32] Meanwhile, these oval-shaped Fe/Fe_3C NPs on the NG support are uniformly coated by a few layers of *in situ* formed GC shells. The thickness of these GC shells ranged from 1.2 to 2.4 nm (4−8 layers of carbon) with an interplanar spacing of 0.334 nm, corresponding to the diffraction peak of C (002). Additionally, the lattice fringe in the core with a distance of 0.191 nm is equal to the (112) plane of Fe_3C, suggesting that a single crystalline Fe_3C exists in Fe-N/G. Similarly, Fe-NG also uniformly spreads Fe/Fe_3C NPs with an average diameter of 22.1 nm and 3−5 layers of GC

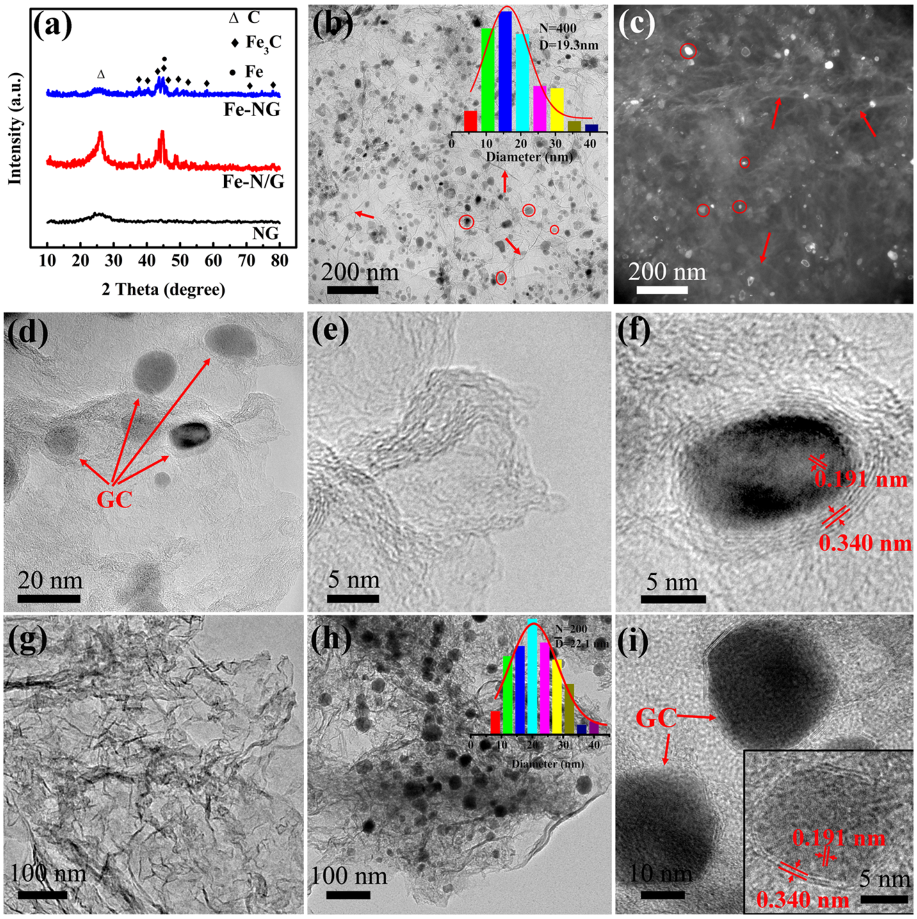

Figure 2. (a) XRD pattern of the prepared NG, Fe-N/G, and Fe-NG catalysts; low-resolution (b) bright-field and (c) dark-field TEM images of Fe-N/G (circle: metal NPs, arrow: graphene); (d−f) high-resolution TEM images of Fe-N/G catalysts; TEM images of (g) NG and (h, i) Fe-NG (inset in (b, h): the size distribution of metal nanoparticles).

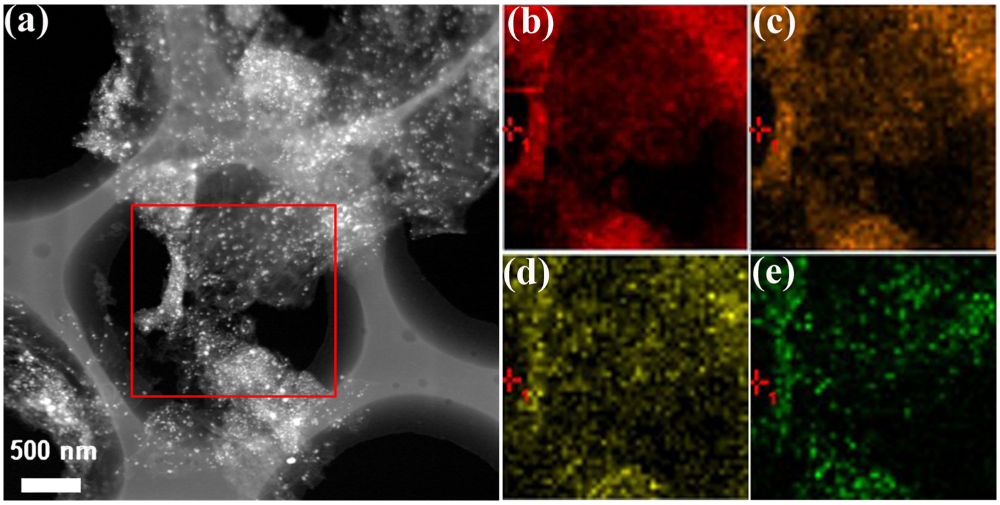

Figure 3. STEM image of Fe-N/G (a) and corresponding element distribution of (b) C, (c) N, (d) O, and (e) Fe for the square region marked in (a).

shells on the surface of NG. The enlargement of NPs' diameter for Fe-NG is probably due to the lack of the strong restriction and dispersion for Fe ions from g-C_3N_4 during the *ex situ* synthesis process.

The scanning transmission electron microscope (STEM) image of Fe-NG in Figure 3a further presents that transparent graphene nanosheets are micrometer in size and homogeneously decorated with Fe/Fe_3C NPs, which is well consistent with the TEM results. Figure 3b−e shows the mapping images of C, N, O, and Fe. It can be found that Fe/Fe_3C NPs are evenly distributed on the surface of graphene in a large range, and a carbon-enriched surrounding is observed around Fe/Fe_3C NPs, which vividly present the carbon coating shells on Fe/Fe_3C NPs. Importantly, the nitrogen concentration around

Table 1. Physical Properties of the Synthesized NG, Fe-N/G, and Fe-NG Catalysts[a]

	graphitic degree I_D/I_G	C/N (atom ratio)	Fe content (wt %)	S_{BET} (m^2/g)	S_{micro} (cm^2/g)	V_{total} (cm^3/g)	average pore size (nm)
NG	1.14	9.43		354	31.0	1.28	14.0
Fe-N/G	0.79	17.21	18.95	393	57.9	0.99	10.6
Fe-NG	0.86	17.42	21.75	388	12.6	1.22	13.4

[a] I_D/I_G: Intensity ratio of D peak and G peak in Raman spectra. C/N (atom ratio): surface atom concentration ratio of C:N calculated form XPS test. S_{BET}: specific surface area calculated according to the BET method. S_{micro}: microporous surface area calculated according to the *t*-plot method. V_{total}: total pore volume. Average pore size (nm) is calculated from the adsorption curve according to the BJH method.

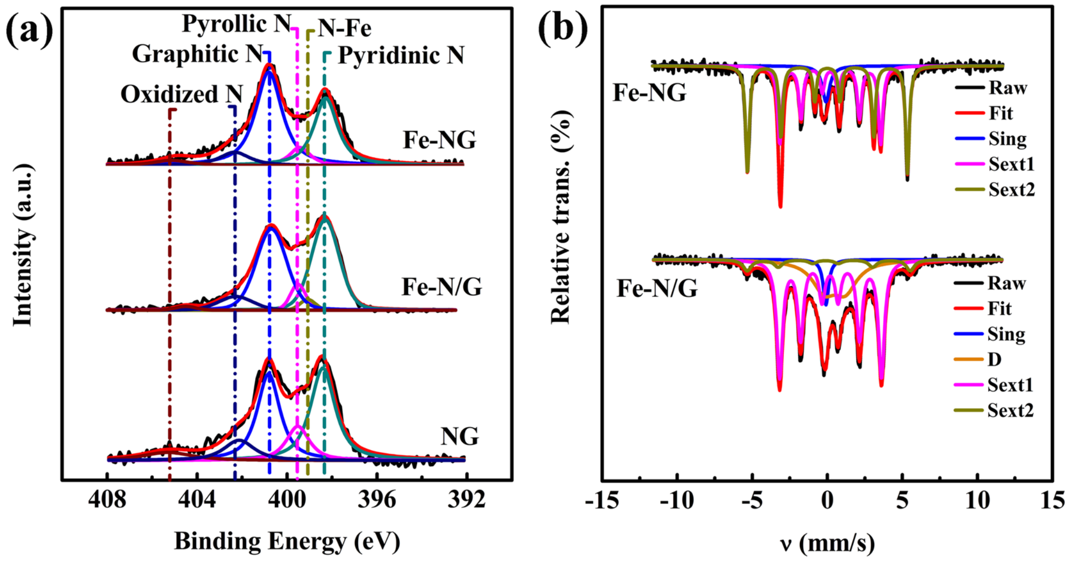

Figure 4. (a) High-resolution N 1s XPS spectra of the prepared NG, Fe-N/G, and Fe-NG catalysts. (b) Mössbauer spectra of the prepared Fe-N/G and Fe-NG catalysts measured at room temperature.

Fe/Fe_3C NPs is also higher than that in graphene (Figure 3e), indicating that Fe-N-C active sites have been successfully generated at the Fe/Fe_3C−GC interface.[33] Furthermore, the loading of Fe on such structures can be simply controlled via adjusting the weight ratio of Fe precursor/glucose. As shown in Figures S3 and S4, the density of Fe/Fe_3C NPs is increased gradually along with the increment of weight ratio from 10% to 40%, while the 2D morophology of Fe-N/G is still kept integrally.

The physical properties of the prepared NG, Fe-N/G, and Fe-NG catalysts are systematically characterized by Raman spectra, nitrogen adsorption/desorption measurements, thermogravimetric analysis (TGA), XPS, and Mössbauer spectra. The results are shown in Table 1 and Figure S2. Raman spectra in Figure S2a show an obvious D-band at around 1335 cm^{-1} that originated from sp^3-hybridized disordered carbon and/or defects and a G-band at around 1575 cm^{-1} from sp^2-hybridized graphitic carbon, respectively, for NG, Fe-N/G, and Fe-NG. Obviously, the I_D/I_G peak intensity ratio of Fe-N/G (0.79) is much lower than those of NG (1.14) and Fe-NG (0.86). Furthermore, the 2D-band peak at 2680 cm^{-1} for Fe-N/G is strengthened and narrowed in comparison with those for NG and Fe-NG. These above results indicate that improved graphitic degree and weakened nanosheet stacking for Fe-N/G can be achieved via the *in situ* synthesis route. On the other hand, nitrogen ad sorption/desorption measurements in Figure S2b show that a typical Type IV isotherm characteristic with an adsorption hysteresis is observed from the sorption curves for NG, Fe-N/G, and Fe-NG, suggesting that plenty of mesopores exist in these samples. Importantly, Fe-N/G has an enhanced specific surface area of 393 m^2/g and a decreased average pore width of 10.6 nm when compared to 354 m^2/g and 14.0 nm for NG, respectively. Likewise, the surface properties of *ex situ* synthesized Fe-NG are also improved (381 m^2/g and 13.4 nm) from NG, although the magnitude is lower than Fe-N/G. Notably, the microporous structure of Fe-N/G (51.9 m^2/g) is greatly increased compared with those of NG (31.0 m^2/g) and Fe-NG (12.6 m^2/g) during the *in situ* synthesis process, which is important for generation of Fe-N active sites.[34]

The Fe content for Fe-N/G and Fe-NG is calculated from the TGA curves in Figure S2c. The relative mass of Fe is close for Fe-NG (18.95 wt %) and Fe-NG (21.75 wt %), while XPS reveals only 0.48 and 0.86 at. % of Fe on the surface of Fe-N/G and Fe-NG, respectively. This result implies that most of the Fe is protected by GC shells, which makes it difficult to be detected by XPS signals.[18] The XPS surveys in Figure S2d show that as high as 9.09 at. % N (C/N: 9.43) is successfully doped into NG, whereas 5.21 at. % (C/N: 17.21) and 5.00 at. % (C/N: 17.42) are doped into Fe-N/G and Fe-NG, respectively. The decrease of nitrogen content for Fe-N/G and Fe-NG suggests that the existence of Fe plays an important role in the doped content for nitrogen, which is probably due to the catalytic graphitization of Fe, promoting the decomposition of nitrogen configurations with weak thermostability.

The high-resolution N 1s XPS spectra are shown in Figure 4a. The N 1s XPS spectra of NG can be deconvolved into four types of nitrogen: pyridinic N (N1 at 398.8 eV, 37.55 at. %), pyrrolic N (N2 at 399.5 eV, 12.92 at. %), graphitic N (N3 at 401.2 eV, 32.56 at. %), and oxidized N (N4 at 402.4 and 404.5 eV, 16.97 at. %).[35] The Fe-NG catalyst has the same types of nitrogen with a corresponding content of 31.53 at. % (N1), 7.45 at. % (N2), 48.68 at. % (N3), and 12.32 at. % (N4), while

Table 2. Mössbauer Parameters for Fe-N/G and Fe-NG Measured at Room Temperature[a]

sample	peak	δ (mm/s)	ΔE (mm/s)	H_{hf} (KOe)	fwhm (mm/s)	area (%)	assign
Fe-N/G	Sing	0			0.20 ± 0.01	5.1	superparam iron
	D	0.58 ± 0.02	1.42 ± 0.04		0.93 ± 0.01	27.9	Fe(II)-N_4/CFe(II)-N_2
	Sext1	0.29 ± 0	−0.03 ± 0	210.3 ± 0.1	0.24 ± 0	59.2	Fe_3C
	Sext2	0.08 ± 0.02	−0.22 ± 0.05	336.7 ± 0.4	0.33 ± 0	7.8	α-Fe
Fe-NG	Sing	−0.04 ± 0.01			0.29 ± 0.01	8.6	superparam iron
	Sext1	0.24 ± 0	0	208.6 ± 0.2	0.17 ± 0	42.0	Fe_3C
	Sext2	0.05 ± 0	0.01 ± 0	330.6 ± 0.1	0.15 ± 0	49.3	α-Fe

[a] δ: Isomer shift. ΔE: Quadrupole splitting. H_{hf}: Half-width hyperfine field.

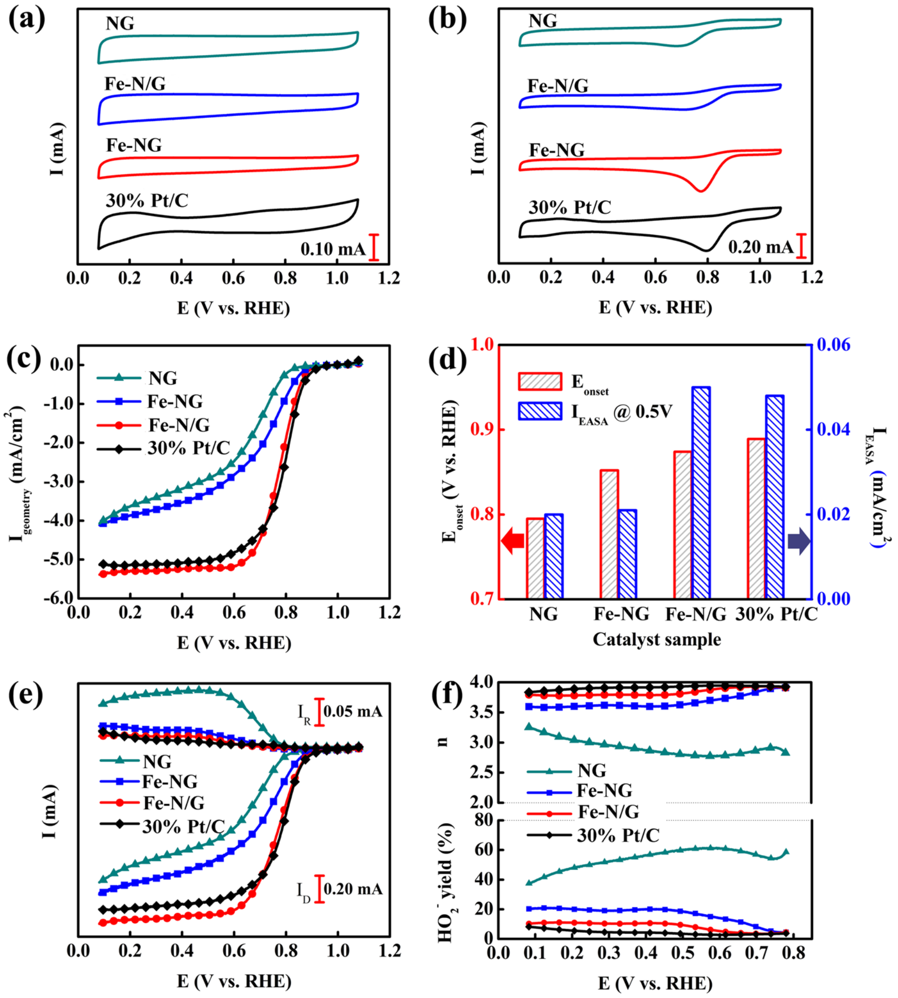

Figure 5. Electrochemical activity and four-electron selectivity of the prepared NG, Fe-N/G, and Fe-NG catalysts. CV curves in (a) N_2- and (b) O_2-saturated 0.1 M KOH solutions with a scan speed of 50 mV/s; (c) RDE LSVs and (d) corresponding ORR onset potential (E_{onset}) and catalytic current density vs electrochemical active surface area (I_{EASA}) at 0.5 V; (e) RRDE LSVs and (f) the dependence of HO_2^- yield and electron transfer number (n).

a new peak at 399.1 eV appears in the Fe-N/G catalyst, assigned to Fe−N bonds. The content is 41.08 at. % (N1), 2.71 at. % (N-Fe), 6.54 at. % (N2), 40.66 at. % (N3), and 9.01 at. % (N4). It can be found that the *in situ* method is beneficial to the generation of Fe-N active sites. Furthermore, the introduction of Fe via the *in situ* or *ex situ* method will promote the relative content of pyridinic and graphitic nitrogen (81.74 at. % for Fe-N/G and 80.21 at. % for Fe-NG vs 70.01 at. % for NG), which are highly active doping types for ORR.[36]

Considering that the state of Fe cannot be detected exactly by the XPS test, Mössbauer spectrum analysis is employed here to precisely analyze the existence state of Fe in the Fe-N/G and Fe-NG catalysts. As shown in Figure 4b, the Mössbauer spectrum of Fe-N/G can be fitted with singlet, doublet, and sextet lines. Table 2 lists their assignments, with the proportions of different Fe species according to the peak areas. Except for the superparam iron (Sing), Fe_3C (Sext1), and α-Fe (Sext2), a doublet is observed in the spectrum, which is assigned Fe(II)-N_4/CFe(II)-N_2.[37] It can be found that as high as 24.1 wt % Fe in the Fe-N/G is bonded to nitrogen atoms, which serve as highly effective active sites for ORR. On the contrary, there is no doublet observed in the Mössbauer spectrum of Fe-NG, suggesting that no Fe−N bond is formed in this catalyst. Therefore, one can believe that the *in situ*

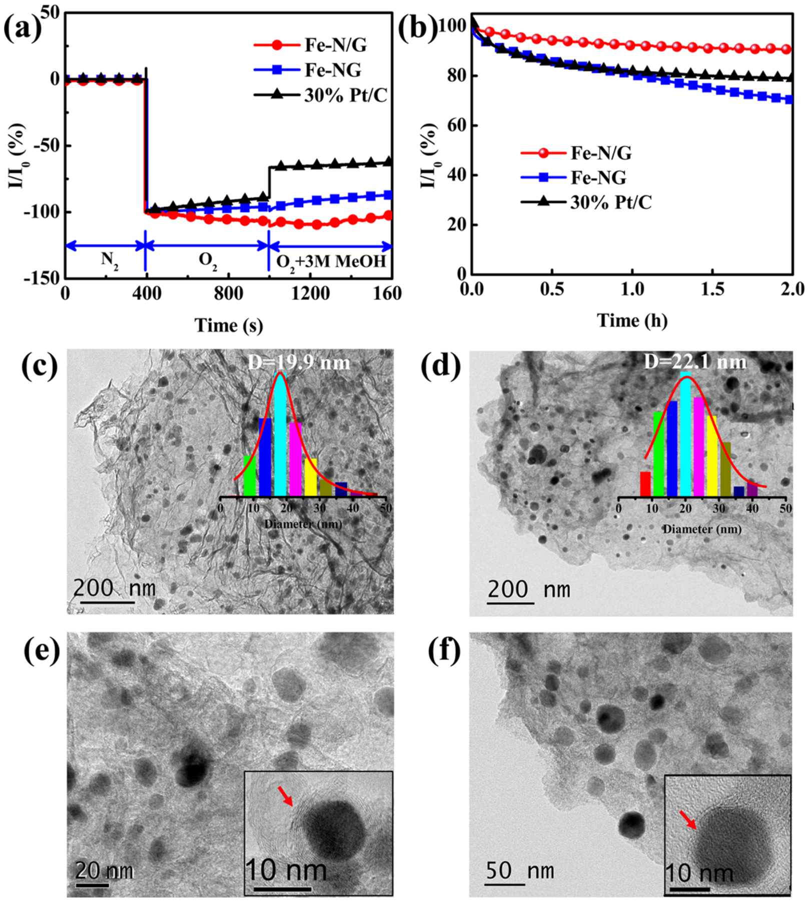

Figure 6. Chronoamperometric responses of Fe-N/G, Fe-NG, and 30% Pt/C at 0.5 V vs RHE in (a) N_2-saturated 0.1 M KOH solutions, followed by addition of saturated O_2 and 3 M methanol successively at 400 s and 1000 s, respectively; (b) current−time responses of Fe-N/G, Fe-NG, and 30% Pt/C at 0.5 V vs RHE in O_2-saturated 0.1 M KOH solution; TEM images of (c, e) Fe-N/G and (d, f) Fe-NG after stability test.

synthesis route has huge advantages over the formation of Fe−N bonds. As a consequence, highly active sites of pyridinic- and graphitic-type doped nitrogen as well as Fe(II)-N_4/CFe(II)-N_2 centers are well integrated in the Fe-N/G catalyst, which is beneficial to cooperatively catalyze the reduction of oxygen.

3.2. Electrocatalytic Performance of the Prepared NG, Fe-N/G, and Fe-NG Catalysts. The electrocatalytic ORR properties of as-prepared NG, Fe-N/G, Fe-NG, and commercial 30 wt % Pt/C catalysts were first characterized using cyclic voltammetry (CV) tests. As shown in Figure 5a, a typical double-layer capacitance performance for high-surface-area carbons without any obvious redox peaks is observed for all catalysts in N_2-saturated 0.1 M KOH solution. By contrast, an apparent cathodic peak appears in the CV curves in Figure 5b when the electrolyte solution is saturated with O_2, which suggests a pronounced electrocatalytic ORR on the as-prepared samples. Notably, compared to NG and Fe-NG, Fe-N/G has a drastically enhanced ORR peak current and peak potential, which nearly approaches or is equal to that of commercial 30 wt % Pt/C.

Rotating disk electrode (RDE) linear sweep voltammetry (LSV) test results in Figure 5c,d demonstrate that the Fe-N/G catalyst achieves an onset potential of 0.874 V vs RHE and a current density (vs geometric area) of 5.21 mA/cm^2 at 0.5 V vs RHE, both of which are much better than that of NG (0.795 V and 2.91 mA/cm^2, respectively) and Fe-NG (0.852 V and 3.27 mA/cm^2, respectively) and comparable to that of 30 wt % Pt/C (0.889 V and 5.03 mA/cm^2, respectively). In order to evaluate the real activity of the catalysts' surface, we calculated roughly the electrochemical active surface area (EASA) of the prepared catalysts based on the electric double-layer capacitance theory, as reported by Zhao et al.[38] The EASA is 28.83, 30.40, 20.46, and 20.64 cm^2 for 10 μg of NG, Fe-NG, Fe-N/G, and 30% Pt/C, respectively (vs ∼2 cm^2 for glass carbon electrode without loading of any catalyst). Then, the obtained catalytic current density vs EASA (I_{EASA}) is 0.020, 0.021, 0.050, and 0.048 mA/cm^2 for NG, Fe-NG, Fe-N/G, and 30 wt % Pt/C. It can be found that the *in situ* synthesis route can significantly enhance the catalytic current as well as onset potential, whereas the *ex situ* synthesis method only makes moderate improvement on onset potential. Meanwhile, we found that the catalyst obtained without addition of glucose possesses an irregular morphology with significant agglomeration, resulting into a very bad electrocatalytic performance (Figure S5). These results suggest that the excellent performance of Fe-N/G is probably ascribed to the formation of novel and efficient Fe(II)-N_4/CFe(II)-N_2 active sites on the highly graphitic and opened graphene framework via the *in situ* route, whereas the *ex situ* method only promotes a small improvement on the graphitic degree as well as surface area of Fe-NG.

To deeply understand the ORR kinetics of the prepared catalysts, LSVs were recorded on a rotating ring disk electrode (RRDE) modified by NG, Fe-NG, Fe-N/G, and 30 wt % Pt/C catalysts. Figure 5e,f clearly shows that the peroxide yield and electron transfer numbers (n) for NG are 38.0−61.9% and 2.7−3.2, whereas a small peroxide yield of below 10.5% and a high n

of above 3.77 are observed for Fe-N/G over the whole potential range from 0.80 to 0.10 V. Even though excess metal loading may slightly decrease the activity (Figure S6), a high catalytic activity and selectivity can still be maintained for the whole Fe-N/G catalysts. On the contrary, the ORR kinetics on Fe-NG is still far from that on Fe-N/G and 30% Pt/C, even though a small improvement is also achieved on it. On the basis of the above results, we can conclude that the excellent activity as well as selectivity for Fe-N/G must be attributed to the synergistic effect from the effectively doped N sites and highly active Fe-N sites. In addition, the Fe/Fe_3C NPs probably play a nonignorable role on the improvement of electrocatalytic performance not via participating in the reaction directly because of the thick coating of GC shells but via enhancing the graphitic degree as well as the structure stability for the carbon framework.

The methanol-tolerance ability and stability of Fe-NG and Fe-N/G were also measured by chronoamperometry. As shown in Figure 6a, 30 wt % Pt/C exhibits an obvious current decay immediately after the injection of 3 M methanol, indicating the occurrence of the methanol oxidation reaction, whereas no noticeable change of current response is observed on Fe-N/G or Fe-NG. The results demonstrate that Fe-N/G or Fe-NG catalyst possesses considerably better tolerance to methanol crossover than Pt/C. On the other hand, after 2 h of reaction at 0.5 V vs RHE in O_2-saturated 0.1 M KOH solution, only 70.7% of the initial catalytic current of Fe-NG toward ORR can be maintained, whereas 90.7% and 79.7% is retained for Fe-N/G and the commercial 30% Pt/C catalyst, respectively. It indicates that the Fe-N/G catalyst has a more excellent stability than Fe-NG and 30 wt % Pt/C.

The Fe-N/G and Fe-NG catalysts after stability tests were further characterized by TEM analysis. As shown in Figure 6c–f, NG nanosheets in Fe-N/G or Fe-NG catalyst separated by Fe/Fe_3C NPs are still well-dispersed without an obvious stacking phenomenon. Meanwhile, the metal NPs with unchanged diameters as well as phase are still well confined in the GC shells for both of them. These results suggest that these metal particles covered with graphitic carbons cannot participate in the catalytic reaction.[39] As for the stability, it is supposed to be the differences of the nitrogen- and iron-doped carbon framework derived from different synthesis routes that determine the stability of resultant catalysts.

4. CONCLUSION

We facilely fabricate well-defined Fe-N/G ORR catalysts via an *in situ* self-sacrificed template route. Fe/Fe_3C@graphitic carbon nanocapsules are uniformly formed on the NG surface to create a highly opened and stable mesoporous framework structure. Furthermore, effectively doped N sites and highly active Fe-N sites are synchronously constructed on such structures, leading to an enhanced synergistic effect for ORR and promising the Fe-N/G catalyst a similar catalytic activity and four-electron selectivity, but superior stability to commercial 30 wt % Pt/C catalysts in 0.1 M KOH solution under the same loading. Notably, the excellent catalytic performance is achieved via such a simple fabrication process using inexpensive, available resources, which can significantly reduce production costs and have huge advantages for large-scale production.

■ ASSOCIATED CONTENT

Ⓢ Supporting Information

The Supporting Information is available free of charge on the ACS Publications website at DOI: 10.1021/acsami.5b05834.

Raman, BET, TGA, and XPS survey of NG, Fe-N/G, and Fe-NG; XRD, Raman, SEM, TEM, and electrochemical characterizations of Fe-N/G with different Fe loadings (PDF)

■ AUTHOR INFORMATION

Corresponding Authors

*E-mail: liangyy403@126.com (Y.L.).
*E-mail: zhiyang@sjtu.edu.cn (Z.Y.).

Notes

The authors declare no competing financial interest.

■ ACKNOWLEDGMENTS

This work was supported by the National Natural Science Foundation of China (Grant No. 21273114), the Natural Science Foundation of Jiangsu Province (Grant No. BK2012791), the Fundamental Research Funds for the Central Universities (Grant No. NE2015003), the “Six Talent Peaks Program” of Jiangsu Province (Grant No. 2013-XNY-010), a Project Funded by the Priority Academic Program Development of Jiangsu Higher Education Institution and the Program for Professor of Special Appointment (Eastern Scholar) at Shanghai Institutions of Higher Learning.

■ REFERENCES

(1) Steele, B. C. H.; Heinzel, A. Materials for Fuel-Cell Technologies. *Nature* **2001**, *414* (6861), 345−352.

(2) Chen, A.; Holt-Hindle, P. Platinum-Based Nanostructured Materials: Synthesis, Properties, and Applications. *Chem. Rev.* **2010**, *110* (6), 3767−3804.

(3) Liu, M.; Zhang, R.; Chen, W. Graphene-Supported Nanoelectrocatalysts for Fuel Cells: Synthesis, Properties, and Applications. *Chem. Rev.* **2014**, *114* (10), 5117−5160.

(4) Morozan, A.; Jousselme, B.; Palacin, S. Low-Platinum and Platinum-Free Catalysts for the Oxygen Reduction Reaction at Fuel Cell Cathodes. *Energy Environ. Sci.* **2011**, *4* (4), 1238−1254.

(5) Debe, M. K. Electrocatalyst Approaches and Challenges for Automotive Fuel Cells. *Nature* **2012**, *486* (7401), 43−51.

(6) Jasinski, R. A New Fuel Cell Cathode Catalyst. *Nature* **1964**, *201* (4925), 1212−1213.

(7) Zhang, G.; Xia, B. Y.; Xiao, C.; Yu, L.; Wang, X.; Xie, Y.; Lou, X. W. General Formation of Complex Tubular Nanostructures of Metal Oxides for the Oxygen Reduction Reaction and Lithium-Ion Batteries. *Angew. Chem., Int. Ed.* **2013**, *52* (33), 8643−8647.

(8) Zhang, G.; Xia, B. Y.; Wang, X.; Lou, X. W. Strongly Coupled $NiCo_2O_4$-rGO Hybrid Nanosheets as a Methanol-Tolerant Electrocatalyst for the Oxygen Reduction Reaction. *Adv. Mater.* **2014**, *26* (15), 2408−2412.

(9) Gong, K.; Du, F.; Xia, Z.; Durstock, M.; Dai, L. Nitrogen-Doped Carbon Nanotube Arrays with High Electrocatalytic Activity for Oxygen Reduction. *Science* **2009**, *323* (5915), 760−764.

(10) Yang, Z.; Yao, Z.; Li, G.; Fang, G.; Nie, H.; Liu, Z.; Zhou, X.; Chen, X. a.; Huang, S. Sulfur-Doped Graphene as an Efficient Metal-Free Cathode Catalyst for Oxygen Reduction. *ACS Nano* **2012**, *6* (1), 205−211.

(11) Liang, Y.; Li, Y.; Wang, H.; Zhou, J.; Wang, J.; Regier, T.; Dai, H. Co_3O_4 Nanocrystals on Graphene as a Synergistic Catalyst for Oxygen Reduction Reaction. *Nat. Mater.* **2011**, *10* (10), 780−786.

(12) Wang, H.; Liang, Y.; Li, Y.; Dai, H. $Co_{1-x}S$−Graphene Hybrid: A High-Performance Metal Chalcogenide Electrocatalyst for Oxygen Reduction. *Angew. Chem., Int. Ed.* **2011**, *50* (46), 10969−10972.

(13) Wang, S.; Iyyamperumal, E.; Roy, A.; Xue, Y.; Yu, D.; Dai, L. Vertically Aligned BCN Nanotubes as Efficient Metal-Free Electrocatalysts for the Oxygen Reduction Reaction: A Synergetic Effect by Co-Doping with Boron and Nitrogen. *Angew. Chem., Int. Ed.* **2011**, *50* (49), 11756−11760.

(14) Zhao, Y.; Yang, L.; Chen, S.; Wang, X.; Ma, Y.; Wu, Q.; Jiang, Y.; Qian, W.; Hu, Z. Can Boron and Nitrogen Co-Doping Improve Oxygen Reduction Reaction Activity of Carbon Nanotubes? *J. Am. Chem. Soc.* **2013**, *135* (4), 1201−1204.

(15) Bashyam, R.; Zelenay, P. A Class of Non-Precious Metal Composite Catalysts for Fuel Cells. *Nature* **2006**, *443* (7107), 63−66.

(16) Wu, G.; More, K. L.; Johnston, C. M.; Zelenay, P. High-Performance Electrocatalysts for Oxygen Reduction Derived from Polyaniline, Iron, and Cobalt. *Science* **2011**, *332* (6028), 443−447.

(17) Wu, G.; Zelenay, P. Nanostructured Nonprecious Metal Catalysts for Oxygen Reduction Reaction. *Acc. Chem. Res.* **2013**, *46* (8), 1878−1889.

(18) Ferrandon, M.; Kropf, A. J.; Myers, D. J.; Artyushkova, K.; Kramm, U.; Bogdanoff, P.; Wu, G.; Johnston, C. M.; Zelenay, P. Multitechnique Characterization of a Polyaniline−Iron−Carbon Oxygen Reduction Catalyst. *J. Phys. Chem. C* **2012**, *116* (30), 16001−16013.

(19) Kattel, S.; Atanassov, P.; Kiefer, B. A Density Functional Theory Study of Oxygen Reduction Reaction on Non-PGM Fe-N_x-C Electrocatalysts. *Phys. Chem. Chem. Phys.* **2014**, *16* (27), 13800−13806.

(20) Xia, B.; Yan, Y.; Wang, X.; Lou, X. W. Recent Progress on Graphene-Based Hybrid Electrocatalysts. *Mater. Horiz.* **2014**, *1* (4), 379−399.

(21) Parvez, K.; Yang, S.; Hernandez, Y.; Winter, A.; Turchanin, A.; Feng, X.; Müllen, K. Nitrogen-Doped Graphene and Its Iron-Based Composite As Efficient Electrocatalysts for Oxygen Reduction Reaction. *ACS Nano* **2012**, *6* (11), 9541−9550.

(22) Peng, H.; Mo, Z.; Liao, S.; Liang, H.; Yang, L.; Luo, F.; Song, H.; Zhong, Y.; Zhang, B. High Performance Fe- and N- Doped Carbon Catalyst with Graphene Structure for Oxygen Reduction. *Sci. Rep.* **2013**, *3*, 1765.

(23) El-Kady, M. F.; Strong, V.; Dubin, S.; Kaner, R. B. Laser Scribing of High-Performance and Flexible Graphene-Based Electrochemical Capacitors. *Science* **2012**, *335* (6074), 1326−1330.

(24) Li, X.-H.; Kurasch, S.; Kaiser, U.; Antonietti, M. Synthesis of Monolayer-Patched Graphene from Glucose. *Angew. Chem., Int. Ed.* **2012**, *51* (38), 9689−9692.

(25) Narita, A.; Feng, X.; Müllen, K. Bottom-Up Synthesis of Chemically Precise Graphene Nanoribbons. *Chem. Rec.* **2015**, *15* (1), 295−309.

(26) Wang, X.; Maeda, K.; Thomas, A.; Takanabe, K.; Xin, G.; Carlsson, J. M.; Domen, K.; Antonietti, M. A Metal-Free Polymeric Photocatalyst for Hydrogen Production from Water under Visible Light. *Nat. Mater.* **2009**, *8* (1), 76−80.

(27) Zheng, Y.; Jiao, Y.; Zhu, Y.; Li, L. H.; Han, Y.; Chen, Y.; Du, A.; Jaroniec, M.; Qiao, S. Z. Hydrogen Evolution by A Metal-Free Electrocatalyst. *Nat. Commun.* **2014**, *5*, 3783.

(28) Datsyuk, V.; Kalyva, M.; Papagelis, K.; Parthenios, J.; Tasis, D.; Siokou, A.; Kallitsis, I.; Galiotis, C. Chemical Oxidation of Multiwalled Carbon Nanotubes. *Carbon* **2008**, *46* (6), 833−840.

(29) Wang, X.; Chen, X.; Thomas, A.; Fu, X.; Antonietti, M. Metal-Containing Carbon Nitride Compounds: A New Functional Organic−Metal Hybrid Material. *Adv. Mater.* **2009**, *21* (16), 1609−1612.

(30) Wen, Z.; Ci, S.; Zhang, F.; Feng, X.; Cui, S.; Mao, S.; Luo, S.; He, Z.; Chen, J. Nitrogen-Enriched Core-Shell Structured Fe/Fe_3C-C Nanorods as Advanced Electrocatalysts for Oxygen Reduction Reaction. *Adv. Mater.* **2012**, *24* (11), 1399−1404.

(31) Sajitha, E. P.; Prasad, V.; Subramanyam, S. V.; Eto, S.; Takai, K.; Enoki, T. Synthesis and Characteristics of Iron Nanoparticles in A Carbon Matrix along with the Catalytic Graphitization of Amorphous Carbon. *Carbon* **2004**, *42* (14), 2815−2820.

(32) Zhang, L.; Xia, Z. Mechanisms of Oxygen Reduction Reaction on Nitrogen-Doped Graphene for Fuel Cells. *J. Phys. Chem. C* **2011**, *115* (22), 11170−11176.

(33) Wu, Z. S.; Yang, S.; Sun, Y.; Parvez, K.; Feng, X.; Müllen, K. 3D Nitrogen-Doped Graphene Aerogel-Supported Fe_3O_4 Nanoparticles as Efficient Electrocatalysts for the Oxygen Reduction Reaction. *J. Am. Chem. Soc.* **2012**, *134* (22), 9082−9085.

(34) Lefèvre, M.; Proietti, E.; Jaouen, F.; Dodelet, J. P. Iron-Based Catalysts with Improved Oxygen Reduction Activity in Polymer Electrolyte Fuel Cells. *Science* **2009**, *324* (5923), 71−74.

(35) Kumar, B.; Asadi, M.; Pisasale, D.; Sinha-Ray, S.; Rosen, B. A.; Haasch, R.; Abiade, J.; Yarin, A. L.; Salehi-Khojin, A. Renewable and Metal-free Carbon Nanofibre Catalysts for Carbon Dioxide Reduction. *Nat. Commun.* **2013**, *4*, 2819.

(36) Yu, D.; Zhang, Q.; Dai, L. Highly Efficient Metal-Free Growth of Nitrogen-Doped Single-Walled Carbon Nanotubes on Plasma-Etched Substrates for Oxygen Reduction. *J. Am. Chem. Soc.* **2010**, *132* (43), 15127−15129.

(37) Hou, Y.; Huang, T.; Wen, Z.; Mao, S.; Cui, S.; Chen, J., Metal−Organic Framework-Derived Nitrogen-Doped Core-Shell-Structured Porous Fe/Fe_3C@C Nanoboxes Supported on Graphene Sheets for Efficient Oxygen Reduction Reactions. *Adv. Energy Mater.* **2014**, *4* (11), .10.1002/aenm.201400337

(38) Zhao, Y.; Nakamura, R.; Kamiya, K.; Nakanishi, S.; Hashimoto, K. Nitrogen-doped Carbon Nanomaterials as Non-metal Electrocatalysts for Water Oxidation. *Nat. Commun.* **2013**, *4*, 2390.

(39) Zhu, Y.; Zhang, B.; Liu, X.; Wang, D. W.; Su, D. S. Unravelling the Structure of Electrocatalytically Active Fe−N Complexes in Carbon for the Oxygen Reduction Reaction. *Angew. Chem., Int. Ed.* **2014**, *53* (40), 10673−10677.